ACSNANO

www.acsnano.org

ARTICLE

Hexagonal Boron Nitride for Sulfur Corrosion Inhibition

Govind Chilkoor, Kalimuthu Jawaharraj, Bhuvan Vemuri, Alex Kutana, Manoj Tripathi, Divya Kota, Taib Arif, Tobin Filleter, Alan B. Dalton, Boris I. Yakobson, M. Meyyappan, Muhammad M. Rahman,* Pulickel M. Ajayan,* and Venkataramana Gadhamshetty*

Cite This: https://dx.doi.org/10.1021/acsnano.0c03625

Read Online

ACCESS | Metrics & More | Article Recommendations | Supporting Information

ABSTRACT: Corrosion by sulfur compounds is a long-standing challenge in many engineering applications. Specifically, designing a coating that protects metals from both abiotic and biotic forms of sulfur corrosion remains an elusive goal. Here we report that atomically thin layers (~4) of hexagonal boron nitride (hBN) act as a protective coating to inhibit corrosion of the underlying copper (Cu) surfaces (~6−7-fold lower corrosion than bare Cu) in abiotic (sulfuric acid and sodium sulfide) and biotic (sulfate-reducing bacteria medium) environments. The corrosion resistance of hBN is attributed to its outstanding barrier properties to the corrosive species in diverse environments of sulfur compounds. Increasing the number of atomic layers did not necessarily improve the corrosion protection mechanisms. Instead, multilayers of hBN were found to upregulate the adhesion genes in *Desulfovibrio alaskensis* G20 cells, promote cell adhesion and biofilm growth, and lower the protection against biogenic sulfide attack when compared to the few layers of hBN. Our findings confirm hBN as the thinnest coating to resist diverse forms of sulfur corrosion.

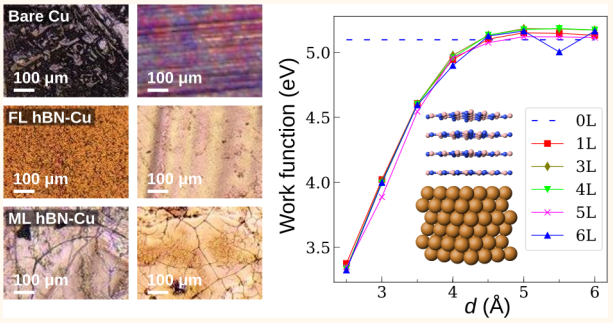

KEYWORDS: *two-dimensional, hexagonal boron nitride, copper, defects, microbial corrosion, density functional theory*

Abiotic corrosion by sulfur compounds compromises a range of metal structures in military applications, the marine sector, the oil industry, utilities, and transportation. For example, airborne sulfur dioxide negatively impacts the safety and readiness of military equipment (e.g., an F-14 aircraft crash due to corrosion of its landing gear), requiring the U.S. to spend $20 billion annually to deal with corrosion issues.[1] Biotic corrosion, commonly termed as microbiologically influenced corrosion (MIC), turns harmless sulfates into aggressive sulfides to degrade copper components of pipelines,[1] transformers,[2] printed circuit boards,[3] and mechanical equipment,[4] all under ambient conditions. Sulfur corrosion is typically controlled by introducing a protective coating layer of polymers such as VOC alkyd, silicone alkyd, polyurethane, latex, epoxy, and polyamides.[5] However, their porous structure renders them susceptible to hydrolysis, degradation, and biogenic sulfide attack. The substantial thickness of polymer coatings may also disrupt the functionality of the underlying metals. Furthermore, biotic corrosion reflects a living machine with the ability to dynamically adjust its physiological environments (e.g., pH, redox potential) and dislodge the passivation layers or attack the C−H bonds in polymer coatings.[6]

Because of the weak coupling to the environment and chemical inertness, two-dimensional (2D) hexagonal boron nitride (hBN) thin coatings show an outstanding ability to withstand harsh chemicals,[7−13] microbes,[14] and heat.[15] Recent advances in growth techniques of large-area hBN coatings are expected to enable their use in commercial applications. The pore size of 2D hBN layers (60 picometer, pm)[16] is also extremely small compared to the effective ionic radii of elemental sulfur (170 pm), sulfide (HS^-) (207 pm),[17] and hydronium (H_3O^+) (99 pm).[18] Also, the electrically insulating characteristics of hBN alleviate the galvanic corrosion issues associated with the graphene coatings.[19] Additionally, hBN atomic layers offer exceptional transparency and do not perturb the optical properties of the underlying metals. The optical reflectivity of Cu at 550 nm changes slightly in the

Received: April 30, 2020
Accepted: October 15, 2020

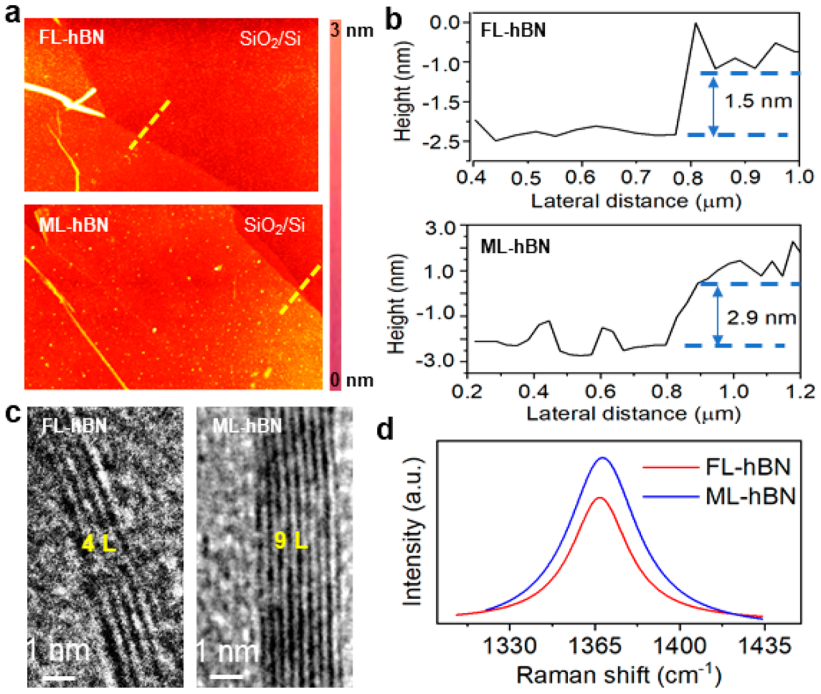

Figure 1. Structural characterization of hBN layers. (a) Atomic force microscope (AFM) images of few-layer hexagonal boron nitride (FL-hBN) and multilayer hexagonal boron nitride (ML-hBN), (b) corresponding height profile for FL-hBN and ML-hBN, (c) TEM images of the synthesized hBN edge revealing that FL-hBN consists of four layers (4L) and the ML-hBN consists of nine layers (9 L). (d) Raman spectra of FL-hBN and ML-hBN.

presence of atomic hBN layers, decreasing from 60.2% for bare Cu to 60.0, 59.4, and 58.4% for 1, 4, and 9 layers of hBN, respectively (Figure S1).

Here, we explore the effectiveness of highly crystalline atomic layers of hBN coatings synthesized via chemical vapor deposition (CVD) for protecting copper against a range of aggressive abiotic and biotic sulfur environments. Although a single-layered hBN can adequately protect underlying metals in both abiotic[13] and biotic[19] environments, it is much easier to enable a rational design and synthesis of multilayered hBN coatings without compromising the mechanical strength and passivation characteristics.[20] We synthesized here a few-layered (FL-hBN) and multilayered hBN (ML-hBN) to understand the effect of number of layers on corrosion protection performance. First, we characterized the CVD-grown coatings via microscopy and spectroscopy techniques. Then, we used electrochemical methods to quantify the corrosion rates and elucidate the mechanism behind the corrosion behavior. We demonstrate that both FL-hBN and ML-hBN coatings offer an excellent ability to control sulfur corrosion in abiotic (aggressive sulfuric acid and sulfides) and biotic environments. Interestingly, FL-hBN provides better resistance to the biogenic sulfide attack in the presence of *D. alaskensis* cells, a genetically tractable strain of sulfate-reducing bacteria when compared to that of ML-hBN. Although the higher number of layers in hBN coatings are expected to enhance the barrier properties, our investigations revealed the unusual behavior of ML-hBN coatings; they cause higher biogenic sulfide attack because of their greater ability to upregulate key genes encoding for cell attachment and biofilm growth. We also studied effects of defects and grain boundaries on the performance of hBN coatings.

RESULTS AND DISCUSSION

Synthesis and Characterization of hBN Coatings. We synthesized FL-hBN (<4 layers) and ML-hBN (4−9 layers) on Cu substrates using CVD techniques described earlier.[21] In typical experiments, nitrogen carrier gas was used to deliver liquid borazine precursor (1−3 sccm) through a bubbler to the CVD chamber (at 750 °C for 30 min) along with 2000 sccm of hydrogen. The coatings were postannealed at 1000 °C for 1 h in the presence of hydrogen and nitrogen gas. We transferred the coatings from Cu foil onto SiO_2/Si substrate using a poly(methyl methacrylate) (PMMA)-assisted method for characterization purposes.[21]

We analyzed the hBN films using atomic force microscopy (AFM) to understand the surface morphology. The ML-hBN and FL-hBN films displayed similar color contrast with SiO_2/Si substrate (Figure 1a). The average thicknesses of FL-hBN and ML-hBN coatings on SiO_2/Si substrate, as determined from the AFM height profile images, were found to be around 1.5 and 2.9 nm, respectively (Figure 1b). The TEM images confirmed the number of layers in FL-hBN and ML-hBN to be ∼4 and ∼9 atomic layers, respectively (Figure 1c). The structure of the films was analyzed by Raman spectroscopy. The Raman spectra for FL-hBN and ML-hBN exhibited a G band corresponding to E_{2g} vibration mode at 1368 and 1365 cm^{-1}, respectively (Figure 1d).[22] More details on thin coatings have been provided in Figure S2. Since polycrystalline Cu was used in this study, a multigrain polycrystalline arrangement of hBN atoms over Cu was obtained during the CVD process (Figure S3). On the basis of the analyses of the AFM topography images along with the force−distance spectroscopy (Figure S3a, b), the FL-hBN grains were in the range of 1−2 μm, whereas ML-hBN grains were in the range of 2−8 μm (Figure S3c, d). The hBN layers included triangle-shaped

https://dx.doi.org/10.1021/acsnano.0c03625
ACS Nano XXXX, XXX, XXX−XXX

crystalline grains, as confirmed by both AFM and TEM dark-field image analysis (Figure S3e, f).

Corrosion Resistance in Abiotic Sulfur Medium. A promising application of the synthesized hBN is its use as an oxidation-resistant coating for copper surfaces in abiotic environments. We exposed the hBN layers synthesized on the underlying Cu surface to sulfuric acid (0.5 M H_2SO_4) to study the corrosion resistance properties.[23] As expected, the bare Cu (Figure 2a) suffered from acid attack and developed a distinct signature of corrosion deposits (Cu sulfates seen as a dark black shade) (Figure 2b). Both FL-hBN-Cu and ML-hBN-Cu retained pristine surfaces (Figure 2b) even after 24 h of prolonged exposure, with just slightly blemished spots on FL-hBN-Cu. Potentiodynamic polarization (PDP) and electrochemical impedance spectroscopy (EIS) analysis confirmed the outstanding barrier properties of the hBN layers in corrosive sulfuric acid medium. The corrosion rates of FL-hBN-Cu (35.25 mpy) and ML-hBN-Cu (33.72 mpy) were ~14-fold lower compared to bare Cu (484 mpy) (Figure 2d and Table S1). The corrosion protection efficiency of both FL-hBN-Cu and ML-hBN-Cu was around 93%. Both protective samples exhibited significantly low anodic current densities compared to bare Cu during the anodic and cathodic potential sweeps (Figure 2d).

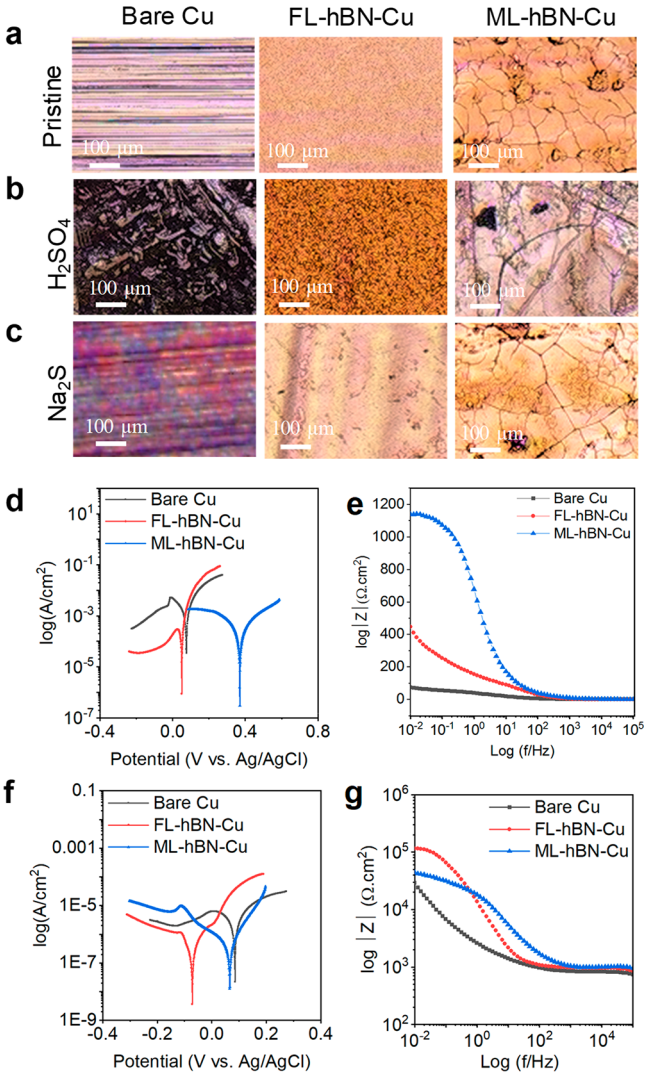

Figure 2. hBN thin coatings against abiotic sulfur corrosion. (a) Optical images of bare Cu, FL-hBN-Cu, and ML-hBN-Cu. (b) Optical images of bare Cu, FL-hBN-Cu, and ML-hBN-Cu exposed to sulfuric acid. (c) Optical images of bare Cu, FL-hBN-Cu, and ML-hBN-Cu exposed to sodium sulfide. Electrochemical analysis of bare Cu, FL-hBN-Cu, and ML-hBN-Cu exposed to 0.5 M H_2SO_4: (d) Tafel plots and (e) Bode plots. Electrochemical study of bare Cu, FL-hBN-Cu, and ML-hBN-Cu exposed to 0.1 M Na_2S: (f) Tafel plots and (g) Bode plots.

Both FL-hBN-Cu and ML-hBN-Cu impeded corrosion by nearly 2 orders of magnitude compared to bare Cu, as seen in the Bode plots of Figure 2e (shown as the *y*-axis intercept at a frequency of 0.01 Hz). Specifically, the corrosion resistance (R_{corr}) of ML-hBN-Cu (1.19 KΩ cm^2) and FL-hBN-Cu (0.542 KΩ cm^2) was ~13-fold and 6-fold higher compared to bare Cu (0.0891 KΩ cm^2), respectively (Table S2). The electrical equivalent circuit (EEC) fitting procedures were used to fit the Bode plot data and determine the R_{corr} values (Figure S4).

Similar to the performance in acidic conditions, both FL-hBN-Cu and ML-hBN-Cu exposed to polysulfide species displayed an exceptional corrosion protection efficiency of 94% (Table S3). Polysulfide compounds are widely implicated in sulfur corrosion issues in petroleum industries. Although the bare Cu exposed to 0.5 M Na_2S developed a signature of corrosion deposits (seen as multicolored strips of blue, silver, and claret red), the FL- hBN-Cu and ML-hBN-Cu surfaces remained intact with no signs of debilitation (Figure 2c). The corrosion rates of FL-hBN-Cu (0.21 mpy) and ML-hBN-Cu (0.29 mpy) were 17-fold and 12-fold lower compared to bare Cu (3.53 mpy), respectively, as determined from the PDP tests (Figure 2f). The EIS data analysis further corroborated the corrosion resistance of hBN coatings (Figure 2g). The R_{corr} for FL-hBN-Cu (274 KΩ cm^2) and ML-hBN-Cu (75.9 KΩ cm^2) was 8- and 2-fold higher than that of bare Cu (32.8 KΩ cm^2), respectively (as seen in the EEC data analysis in Figure S4 and Table S4).

Corrosion Resistance against Biotic Sulfur Medium. We assessed biogenic sulfide attack on Cu by planktonic *D. alaskensis* cells as well as their biofilm counterparts (i.e., sessile cells). Our results reveal that atomic layers of hBN form a formidable barrier between atop *D. alaskensis* cells and underlying Cu surfaces. After 48 h of the exposure to planktonic cells, the FL-hBN-Cu retained its original Cu shine, whereas bare Cu suffered a distinct biogenic sulfide attack (seen as black discolorations) (Figure 3a). The intensity of corrosion products on bare Cu was significantly higher than the protective layer cases (Figure 3b). To visualize the attack on the actual Cu surface, we scraped off the biofilm debris and then performed optical image analysis of the Cu surfaces. As shown, the Cu surfaces modified with the atomic hBN layers retained their physical integrity (Figure 3c), whereas the bare Cu inherited the signature of microbiologically influenced corrosion (MIC).

Both FL-hBN and ML-hBN effectively shielded the Cu surfaces from MIC effects of atop *D. alaskensis* cells (48 h of exposure) and their sessile counterparts (650 h of exposure) (Figure 3d). A larger diameter loop in the Nyquist plot for both cases compared to bare Cu confirm the ability of hBN layers to control MIC (Figure 3e). The R_{corr} for FL-hBN-Cu (123.6 KΩ cm^2) and ML-hBN-Cu (145.4 KΩ cm^2) was significantly higher compared to bare Cu (79.6 KΩ cm^2), as determined using the EEC fitting analysis (Table S5). The MIC rates of FL-hBN-Cu (0.04 mpy) and ML-hBN-Cu (0.05

https://dx.doi.org/10.1021/acsnano.0c03625
ACS Nano XXXX, XXX, XXX−XXX

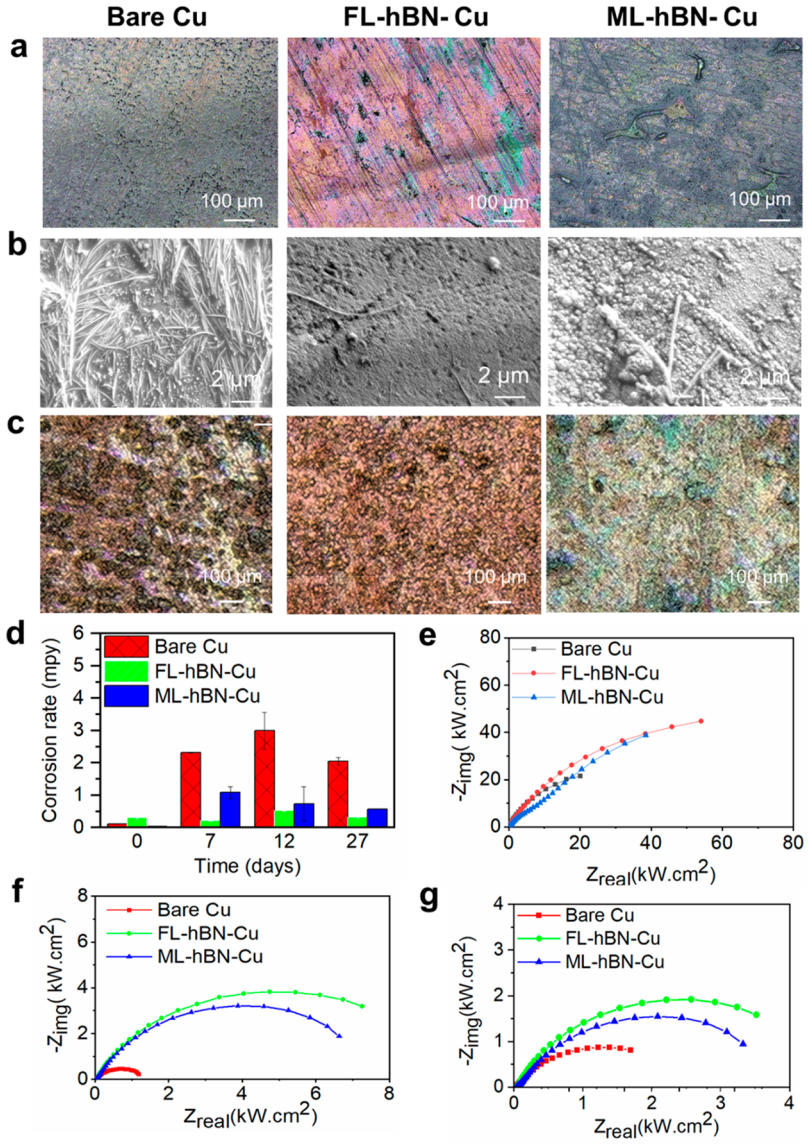

Figure 3. hBN thin coatings against biotic sulfur corrosion (biogenic sulfide attack). (a) Optical images after 48 h of exposure of planktonic cells. (b) Higher magnification SEM images after 48 h of exposure of planktonic cells. (c) SEM images show extensive pitting on bare Cu compared to FL-hBN-Cu and ML-hBN-Cu. (d) Corrosion rates for 27 days of the exposure period in sessile condition. Nyquist plots on (e) day 0 (planktonic, t < 2 h) (f) day 14 and (g) day 27 using a sinusoidal AC potential of 10 mV in the frequency range of 0.01 to 1 × 10^5 Hz.

mpy) were an order of magnitude lower than bare Cu (0.1 mpy), as determined from the LPR tests. LPR tests and EIS analysis confirm that both FL-hBN and ML-hBN layers suppress the MIC by 2.5- to 6-fold throughout the exposure period (examples shown for days 7, 12, and 27, Figure 3d).

Mechanisms of Corrosion Resistance. Our final goal is to elucidate the mechanism of corrosion resistance behavior of the hBN coatings. It is well-known that the cathodic reduction of oxygen (eq 3) influences the degree of Cu corrosion (eq 2). Noting that the hBN-Cu surfaces exposed to sulfuric acid offered higher charge transfer resistance (Figure 2e) and lower corrosion rates (Figure 2d), we attribute the protection mechanism to the outstanding ability of hBN atomic layers to restrict oxygen and protons (eq 1) from reaching the Cu/electrolyte interface (eq 2). The AA′ stacking in the hBN layers aligns to improve the electron cloud density that disfavors the permeation of oxygen and charged protons.[24] The pore size of atomic layers in the coatings are also small enough to restrict permeation of HS^- species, restricting the formation of chalcocite compounds (Cu_2S) (eq 2)[25] and the overall Cu corrosion.

$$O_2 + 4H^+ + 4e^- \rightarrow 2H_2O \quad (1)$$

$$2Cu + HS^- + OH \rightarrow Cu_2S + H_2O + 2e^- \quad (2)$$

After establishing the corrosion resistance of atomic hBN layers on Cu under a range of sulfur corrosion conditions, we assessed the degree of performance improvement due to the higher number of hBN atomic layers in ML-hBN. We report that abiotic sulfur corrosion protection of ML-hBN-Cu is only slightly better than FL-hBN-Cu. Although the R_{corr} value for ML-hBN-Cu (1.19 KΩ cm^2) was 2-fold higher compared to FL-hBN-Cu (0.542 KΩ cm^2), their corrosion rate and protection efficiency were quite the same. We observed similar protection efficiencies (~94%) in the polysulfide environments for both the FL-hBN and ML-hBN coatings (Table S2).

https://dx.doi.org/10.1021/acsnano.0c03625
ACS Nano XXXX, XXX, XXX−XXX

Although counterintuitive, we report superior performance of FL- hBN compared to ML-hBN on Cu exposed to biofilms for a prolonged period. The MIC rate of FL-hBN-Cu (0.52 mpy) was 2-fold lower than that of ML-hBN-Cu (1.08 mpy). The MIC rates for FL-hBN-Cu increased slightly until day 12 and stabilized at 0.31 mpy on day 27, whereas, the MIC rates of ML-hBN-Cu increased from 0.04 mpy (day 0) to 1.08 mpy (day 7) and reached nearly 1.57 mpy on day 27. The EIS results also corroborated better performance of the FL-hBN-Cu. The FL-hBN-Cu displayed a larger diameter Nyquist loop compared to ML-hBN-Cu, both on day 14 (Figure 3f) and Day 27 (Figure 3g). The R_{ct} or charge transfer resistance values for FL-hBN-Cu on days 14 and 27 were 15 and 9% higher than that of ML-hBN-Cu, respectively (Tables S6 and S7), as determined from the EEC fitting analysis of the Nyquist data (Figure S4a). After 27 days of the exposure period, the protection efficiency of FL-hBN-Cu remained at 93%, whereas that of ML-hBN reduced to 35%. Although the thicker hBN coatings offer more tortuous pathways and restrict corrosive metabolites from reaching the underlying Cu surfaces, the ML-hBN-Cu surprisingly suffered from a higher degree biogenic sulfide attack.

To understand the protection mechanisms from various sulfur corrosive species, we performed a computational study based on density functional theory (DFT). Figure 4 shows the

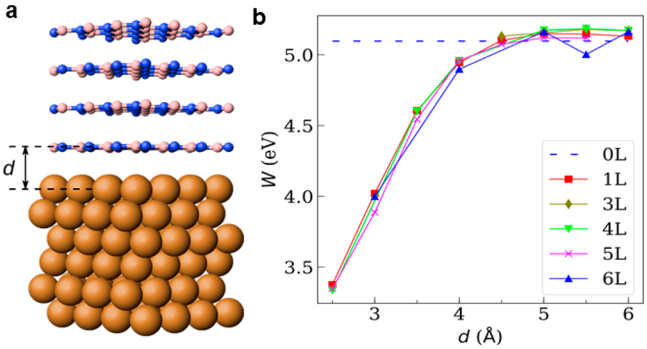

Figure 4. Work function of bare Cu and hBN-coated Cu surfaces showing the barrier properties of hBN against oxidation. (a) Atomistic model for FL-hBN on Cu (111) used in DFT calculations. Brown, blue, and pink spheres mark Cu, N, and B atoms, respectively. (b) Calculated work function (*W*) of Cu (111) surface with adsorbed few-layer (1−6 layers) hBN as a function of hBN-Cu distance (*d*). Dashed blue line shows the work function of bare Cu (111).

atomic configuration and calculated work function (WF) of Cu (111) surface with adsorbed hBN (1−6 layers). A geometry of a 4-layer hBN on Cu with hBN distance fixed at d = 3.5 Å is shown in Figure 4a. The Cu (111) surface was represented by 6 layers of Cu atoms, whereas the hBN layers were arranged in the eclipsed (AA′) stacking.[26] We studied the formation of the electric double layer on the Cu surface after depositing hBN atomic layers. Negative (positive) charges acquired by Cu (hBN) will facilitate the donation of electrons by Cu, shifting the balance in eq 4 toward the formation of chalcocite compounds (Cu_2S), enhancing Cu corrosion. The charging of the double layer will influence the WF of hBN-Cu. The obtained WF dependence on the hBN-Cu distance is shown in Figure 4b. The WF of Cu is not affected by hBN at large Cu-hBN distances d > 4.5 Å. This is not surprising given the absence of any long-range charge transfer between the two materials. The Fermi level of Cu is at −5.1 eV and falls into the bandgap of hBN, for which the values of −6.1 eV for valence band maximum (VBM) and −1.4 eV for conduction band minimum (CBM) were obtained, precluding any flow of free charges. A high ionization potential of hBN hinders the donation of electrons by this material. The formation of a double electric layer at small Cu-hBN distances (d < 4.5 Å) is due to chemical interactions of Cu and hBN as well as Pauli repulsion between occupied hBN and Cu orbitals, pushing the electronic cloud into the metal. Electrons are transferred to Cu, lowering its surface WF and making Cu more electropositive. There is no significant dependence in the distance behavior on the number of hBN layers, indicating that most likely only the outer hBN layer interacts with the metal surface, whereas other layers remain inert, providing mechanical protection against oxidizing species. Although the WF of hBN-Cu(111) is lowered significantly at small hBN-Cu distances, potentially enhancing Cu corrosion, the lowering is most likely inconsequential, as oxidizing species will not be able to access the space between the two materials at d < 4.5 Å. At distances d > 4.5 Å, all hBN layers become inert and will serve as an effective physical barrier against oxidation.

Next, we explored the corrosion protection mechanism for corrosion resistance of hBN in biotic environments. The atomic hBN layers neither restricted the cell attachment (Figure S5) nor the biofilm growth (28 days old rod-shaped biofilm) (Figure 5a). To examine the degree of cell adhesion, we stained *D. alaskensis* cells on bare Cu, FL-hBN-Cu, and ML-hBN-Cu with a green fluorescent SYTO-9 nucleic acid dye. Compared to FL-hBN-Cu, ML-hBN-Cu experienced higher biofilm growth. The cell attachment on ML-hBN-Cu (33% coverage) was 1.6-fold higher compared to bare Cu (21% coverage) after 24 h of exposure. Upon prolonged exposure for 27 days, the bare Cu surface developed 61% coverage (0−15 μm thick biofilm) and FL-hBN-Cu showed 91% coverage (0−15 μm thick biofilm). In contrast, ML-hBN-Cu displayed a bimodal mix: 53% coverage (5−35 μm thick biofilm) and 38% coverage (0−15 μm thickness) (Figure 5b). The higher degree of cell adhesion yielded thicker biofilms on ML-hBN-Cu surfaces. These results suggest that the FL-hBN-Cu surfaces were characterized by a lower degree of biogenic sulfide products (e.g., HS^- and chalcocite).[27]

The differences in the number of layers yielded differences in atomic-scale properties of the coated Cu surfaces, influencing the adhering state of *D. alaskensis* cells, biofilm phenotypes, and the degree of biogenic sulfide attack. Both protective coatings exhibited topographical differences at a nanoscale, as determined by the analysis of the AFM contact mode images (Figure 5c). The roughness of ML-hBN-Cu (4006 ± 1101 pm) was ∼5-fold higher than FL-hBN-Cu (849 ± 170 pm) (Figure S6). Generally, the rougher the surface, the higher the cell adhesion.[28,29]

Wettability of Cu surfaces is another nanoscale surface property that can be influenced by the number of hBN layers. The pristine form of ML-hBN-Cu displayed a higher value of static water contact angle (WCA) (93.5°) compared to FL-hBN-Cu (86.2°) and bare Cu (82.3°) (Figure 5d). The ML-hBN coatings enhanced the hydrophobicity of underlying Cu surfaces, which is known to encourage biofilm growth and associated biogenic sulfide attack. On a related note, hydrophobic surfaces are desirable in abiotic sulfur corrosion applications, as they are known to protect Cu from aggressive chemical species.[30]

https://dx.doi.org/10.1021/acsnano.0c03625
ACS Nano XXXX, XXX, XXX−XXX

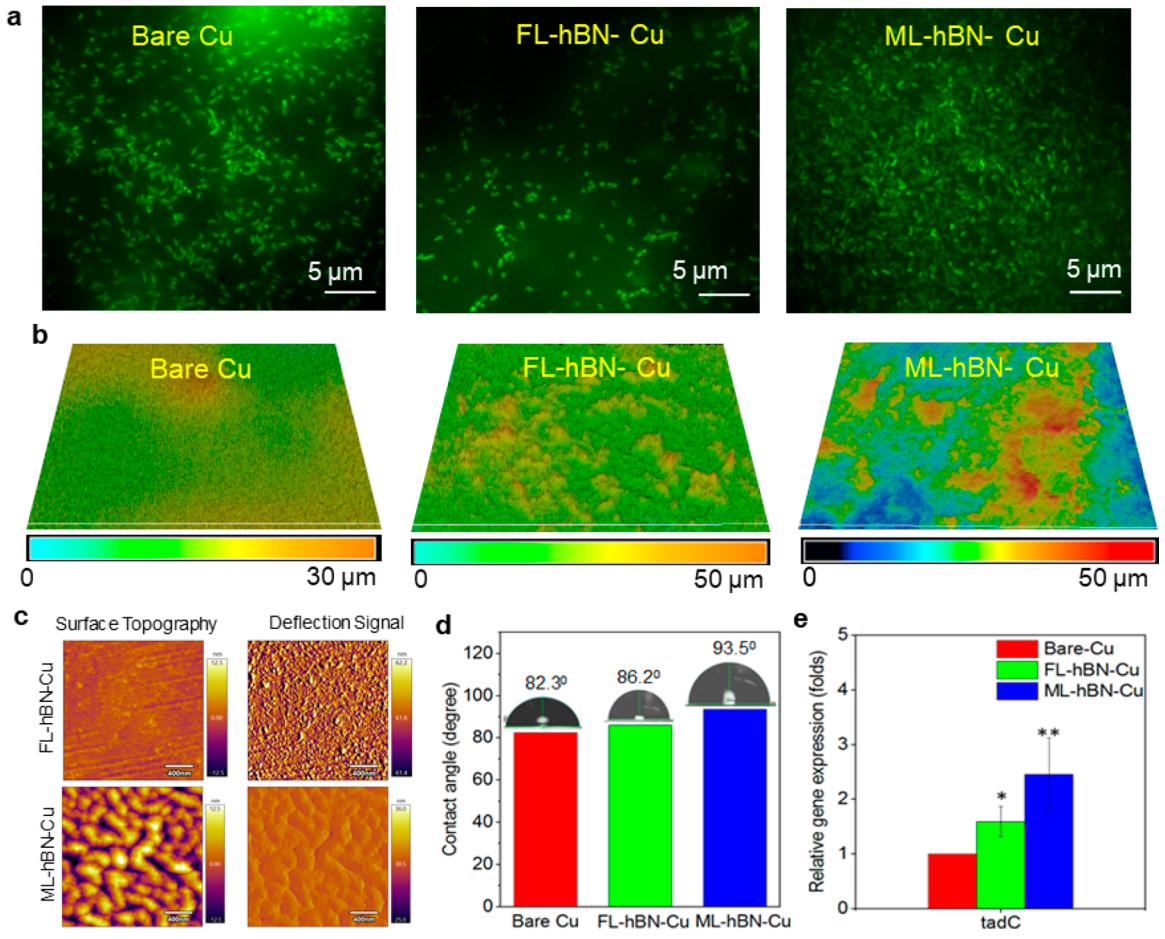

Figure 5. Fluorescent, 3D laser scanning, atomic force microscopy, contact angle measurement, and relative gene expression showing lower cell adhesion on FL-hBN-Cu compared to bare Cu and ML-hBN-Cu. (a) Fluorescence microscope image of total cells obtained after 48 h exposure by staining the surfaces with SYTO 9 green-fluorescent nucleic acid showing lowered adhesion of *D. alaskensis* population adhered to the surface of FL-hBN-Cu compared to bare Cu and ML-hBN-Cu. (b) 3D biofilm thickness profile for bare Cu, FL-hBN-Cu, and ML-hBN-Cu after 27 days of exposure in sessile conditions. (c) AFM surface topography and normal cantilever deflection signal for ML-hBN-Cu and FL-hBN-Cu. (d) Contact angles for bare Cu, FL-hBN-Cu, and ML-hBN-Cu. (e) Relative gene expression (in folds) of *tadC* gene among biofilm of *D. alaskensis* grown on bare-Cu, FL-hBN-Cu, and ML-hBN-Cu. Data represent the mean of triplicates. (Asterisk represents a significant difference $^{**}P < 0.01$; $^{*}P < 0.05$).

We establish that the differences in nanoscale surface properties caused by the differences in the number of layers control the gene expression and genetic responses of "surface-adhering" *D. alaskensis* cells. Our results based on the reverse transcriptase-polymerase chain reaction (RT-PCR) tests revealed a differential gene expression profile of the *tadC* (Flp pilus assembly protein) gene of the *D. alaskensis* biofilm on bare Cu, FL-hBN-Cu, and ML-hBN-Cu surfaces (Figure 5e), based on the cycle threshold values. We report that ML-hBN-Cu triggered an up-regulation of the *tadC* by 2.5 ± 0.7-fold ($P < 0.01$) and FL-hBN-Cu by 1.6 ± 0.3-fold ($P < 0.05$) compared to bare Cu. This Pilus assembly protein promotes cell-to-cell interaction, heterogeneities in biofilm,[31] and corresponding biogenic sulfide attack by *D. alaskensis* cells.[32] The extracellular polymeric substrate (EPS) promotes irreversible cell attachment, metal-binding capacity, and corresponding electron transfer processes that drive the MIC process.[33,34] These results explain why the ML-hBN-Cu surfaces encouraged thicker biofilms and enhanced biogenic sulfide attack compared to FL-hBN-Cu.

Effect of Defects on the Corrosion Protection of Atomic hBN Layers. We have studied the effects of the grain boundaries (GBs) and point defects on the corrosion protection performance of atomic hBN layers. To understand the effect of GBs, we transferred the CVD-grown hBN crystals from FL-hBN-Cu onto Si-SiO_2 using the PMMA transfer method. Then, a specific region of FL-hBN/Si-SiO_2 sample was exposed to 1 M H_2SO_4, a typical corrodent found in MIC environment, for 2 h. We analyzed the topographic surfaces of pristine and corrosive regions of hBN using Kelvin probe force microscopy. We chose FL-hBN for the analysis as they were characterized by smaller grains (Figure S3) and can be expected to yield a greater number of GBs. Our study revealed that GBs undermine the overall performance of atomic hBN layers in corrosive environments (Figure 6a–d and Figure S7). Upon exposure to the H_2SO_4, the surface potential map of the FL-hBN underwent a significant change. The WF of the GB (~4.49 eV) was lower than that of the grain (~4.55 eV). The lower the WF the more active the electrons and more their participation in the electrochemical processes influencing corrosion. Upon exposure to the H_2SO_4 corrodent, the GBs displayed a greater shift in WF (4.49 to 4.72 eV; $|\Delta WF|=0.23$ eV) compared to the grain or basal plane (4.55 to 4.44 eV; $|\Delta WF|=0.11$ eV) (Figure S7d). The higher the ΔWF, the

https://dx.doi.org/10.1021/acsnano.0c03625
ACS Nano XXXX, XXX, XXX−XXX

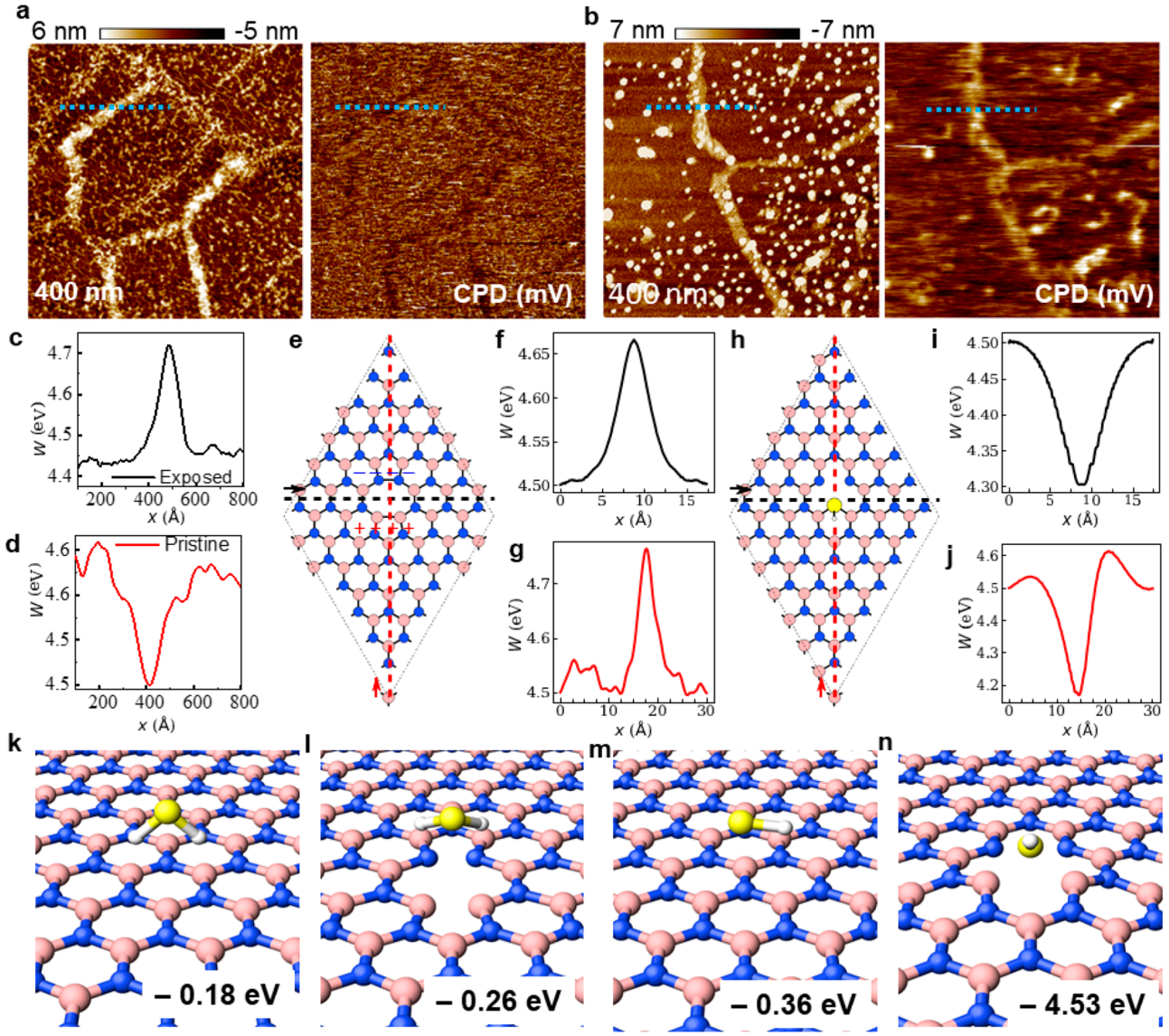

Figure 6. Effect of defects on the corrosion protection of atomic hBN layers. Morphology and surface potential map of (a) pristine FL-hBN/Si-SiO_2 show the topography of a grain region surrounded by GB. (b) FL-hBN/Si-SiO_2 exposed to 1 M H_2SO_4 show the hBN layers impacted by SO_4^{2-} salts and its distinct surface potential compared to surrounding hBN. Measured work function (WF) line profile along the GB for the (c) exposed and (d) pristine region as dash marked in panels a and b. The WF profile reveals the transformation of the WF associated with a drop in carrier concentration at exposed GB compared to the unaffected region. (e) Local WF calculations near point defects in double vacancy of hBN by DFT. (f) WF along dashed horizontal line and (g) WF along dashed vertical line in (e) at a distance of 3 Å from the hBN plane (h) Local WF calculations with sulfide radicals (HS) near a double vacancy in hBN. (i) WF along a dashed horizontal line and (j) work function along a dashed vertical line in (h) at a distance of 5.5 Å from the hBN plane. Adsorption geometries and energies of sulfides on the basal plane of hBN for (k) H_2S on pristine hBN, (l) H_2S near a double vacancy in hBN, (m) HS on pristine hBN, (n) HS near a double vacancy in hBN.

greater the change in the electron concentration and higher the modulation in Fermi energy level.[35] Thus, the GBs favor interactions between the hBN crystals and corrosive entities, undermining the overall corrosion protection.

Point defects in atomic hBN layers can locally change their WF, which in turn could impact the corrosion resistance. We have studied the influence of a double vacancy in a SL-hBN as a model for the point defect by density functional theory (DFT) simulations (Figure 6e–j). The electrostatic potential distribution was calculated near the hBN double vacancy with and without the adsorbed sulfide radical (HS•). The height of the local peak of the electrostatic potential distribution near the hBN double vacancy was found to be ~200 meV at 3 Å above the plane. In the presence of sulfide species, the peak height increased to ~400 meV. These results indicate that the vacancy dipole changes the local WF and influences the corrosion resistance of atomic hBN layers.

We hypothesize that the defects including vacancies and grain boundaries in 2D materials are more reactive compared with their pristine counterparts. To understand the reactivity of the HS• radicals with hBN basal planes with and without vacancy, we have utilized the DFT simulations (Figure 6k–n). Our DFT calculations revealed an increased adsorption energy of sulfur compounds (MIC products) at the defective sites. The adsorption energy of H_2S on pristine hBN (~0.18 eV) was smaller compared to that near a double vacancy (~0.26

https://dx.doi.org/10.1021/acsnano.0c03625
ACS Nano XXXX, XXX, XXX–XXX

eV). Also, the adsorption energy of the HS• radical on defective hBN was more prominent compared to pristine hBN. The energy in pristine hBN was ~0.36 eV, whereas the radical interacts strongly with the double vacancy, evident from higher adsorption energy of ~4.53 eV. Although individual adsorption energies and reactivities may vary depending on the nature of the adsorbates and defects, this general trend of increasing adsorption energy near defects is robust and should apply to other forms of sulfides and other types of defects. These results agree well with the prior reports that the line and point defects such as grain boundaries, edges, vacancies, and substitutional atoms can increase hBN reactivity and degrade its performance.[36]

Integrity of Atomic hBN Layers Exposed to Corrosive Environments. We have carried out a post-mortem analysis of the transferred hBN layers exposed to abiotic and biotic corrosion, using Raman spectroscopy in a range of 1250−1450 cm^{-1} Raman shift and AFM imaging (Figure S8). The Raman spectra revealed that the hBN layers remained intact at the end of both the biotic and abiotic corrosion tests. The retained integrity of the exposed hBN layers was corroborated by the AFM imaging, where the topographic profile of both the grain and GB was found to remain unaltered after the exposure (Figure S8b). However, the exposed hBN layers experienced the phonon softening due to the convolution of strain and doping by metabolites (biotic corrosion) and sulfur salts (abiotic corrosion), as evident from the systematic red shift of hBN E_{2g} peak (Figure S8a).

CONCLUSIONS

In summary, we demonstrate that atomic hBN layers lower copper corrosion by a minimum of 12-fold under a range of abiotic and biotic sulfur environments. Increasing the number of atomic layers did not necessarily improve the performance of hBN coatings against abiotic sulfur corrosion. However, the differences in the number of atomic layers of hBN influenced nanoscale surface properties, which influenced the overexpression of adhesion genes responsible for cell attachment, biofilm growth, and biogenic sulfide attack. The nanoscale defects including grain boundaries and point defects influenced the corrosion protection performance of atomic hBN layers under both the environments. Overall, few atomic layers of hBN show promise for restricting the diffusion of a range of aggressive sulfur species, which represents the rate-limiting step for sulfur corrosion.

METHODS

Characterization of CVD-Grown hBN Coating. The quality of CVD-grown hBN coatings was assessed using optical microscopy, Raman spectroscopy, transmission electron microscopy (TEM), TEM dark-field imaging, and atomic force microscopy (AFM). The hBN films were transferred on to a SiO_2/Si wafer for all of the above analyses except for TEM, which used a lacey carbon-coated grid. A Carl Zeiss Axio vision optical microscope with the following specification was used to obtain the image: Zeiss Axio Cam MRC 5 camera operated in a bright field mode, an objective lens of 10XHD-DIC with a numerical aperture of 0.25 mm and coverslip thickness of 0.17 mm. Axiovision SE64 software was used to process the optical images.

We used the PMMA-transfer method to prepare the samples for the TEM dark-field imaging. FL-hBN-Cu or ML-hBN-Cu was spin coated with PMMA, heat treated and immersed in copper etchant (Transene, CE-100). The hBN films were then transferred onto a SiO_2/Si wafer or carbon-coated Cu grid. The wafer and grid were rinsed thrice with acetone and distilled water to remove the PMMA impurities.

The number of layers of hBN was determined using Raman spectroscopy. Raman spectra were collected using ffTA Foram X3 module (Foster + Freeman Ltd., Evesham, UK) at 532 nm laser excitation with 20x optical lens. A high-resolution TEM (JEM-2100 LaB6) was used to obtain lattice fringes for film edges and selected area (electron) diffraction (SAED) patterns. The thickness of hBN films was measured using the Bruker Multimode-8 AFM system. The scans were carried out in noncontact mode with a ScanAsyst-Air-HR probes having a 2 nm nominal radius. For post-mortem analysis of hBN films exposed to corrosive environments, Raman spectroscopy (spectral resolution 0.8 cm^{-1}) has been carried out using a 532 nm laser line (type: solid-state, model RL53250) using a 100× optical lens by Renishaw inVia. The laser power-up of ~10% (around 1.6 mW) was used for the exposure duration of 10 s using grating 2400 mm/l. The E_{2g} Raman peaks obtained were fitted using the Pseudo Voigt function to measure the peak positions. The Kelvin probe force microscopy (KPFM) characterization was carried out using an AFM-Bruker Dimension Icon (details are provided in the Supporting Information).

To determine the crystallographic orientation of Cu substrates used for growing hBN films, we performed electron-backscatter diffraction (EBSD) measurements using JEOL 7000F Analytical SEM with HDL Technology EBSD at a probe current of 5 nA, an accelerating voltage of 20 kV, and an angle of incidence of 70°. The data for the inversed pole figure was analyzed using Mambo software. We measured the static contact angle to establish the wettability of various substrates using an automated Ramé−Hart 500 digital goniometer equipped with CCD camera (Ramé-hart instrument Co., NJ, USA) at room temperature (~70 °F). A 1 μL droplet of deionized water was placed on a flat horizontal substrate (bare Cu, FL-hBN-Cu and ML-hBN-Cu) using a needle to create a sessile drop, and the angle between the baseline of the drop and the tangent at the drop boundary was measured by a CCD camera connected to the manufacturer's contact angle software (DROPimage Advanced program). The readings for every angle measurement were taken ten times and three drops were measured for every sample.

Friction force microscopy was carried out on the FL-hBN and ML-hBN samples using the Asylum MFP 3D AFM. The root-mean-square surface roughness for both the nanoscale coatings was performed over a 500 × 500 nm area and at a relative humidity of 10%.

SRB Inoculation and Cultivation. *D. alaskensis* cells was initially grown in lactate-C medium[1] with the following components (g/L): sodium lactate, 6.8; sodium sulfate, 4.5; sodium citrate, 0.3; dehydrated calcium chloride, 0.06; ammonium chloride, 1.0; magnesium sulfate, 2.0; potassium phosphate monobasic, 0.5; yeast extract, 1.0; ascorbic acid, 0.1; sodium thioglycollate, 0.1. Prior to inoculation, the culture medium was sterilized at 121 °C for 30 min and deoxygenated with filter-sterilized N_2 gas for 30 min at 15 psi. *D. alaskensis* cultures were then grown in 150 mL serum bottles containing 100 mL of lactate-C medium. The bottles were sealed with butyl rubber stoppers and the initial headspace composition was maintained at 95% N_2 (v/v) and 5% H_2 (v/v). *D. alaskensis* cultures were incubated at 30 °C and 125 rpm on an orbital platform shaker for 48 h.

Biogenic Sulfide Corrosion Experiments. Ten milliliters of *D. alaskensis* culture (1×10^6 cells/mL) from the exponential phase was used to inoculate 400 mL of lactate C medium in the corrosion cell under anaerobic conditions. A Reference 600 Gamry potentiostat (Warminster, PA, USA) was used for all the electrochemical corrosion tests discussed in this study. The corrosion cell consisted of a working electrode (WE) (Bare Cu, FL-hBN-Cu or ML-hBN-Cu), counter electrode (graphite plate), and a reference electrode (Ag/AgCl) in a reference bridge tube. The bare Cu, FL-hBN-Cu, or FL-hBN-Cu sample was laterally mounted on a stainless-steel bracket using an electroplating tape (Φ = 11.3 mm). The exposed surface area of the WE was limited to 1 cm^2. Standard microbiology practices and sterile techniques were used to maintain the axenic cell population during the experiments. The corrosion cell having the lactate C medium was

https://dx.doi.org/10.1021/acsnano.0c03625
ACS Nano XXXX, XXX, XXX−XXX

initially purged with sterile nitrogen gas at 15 psi for 30 min to develop anaerobic conditions. Then *D. alaskensis* culture inoculum (10% v/v) with an initial cell number concentration of 1×10^5 cells/mL was transferred into the corrosion cell. An SRB test kit was used to measure the concentration of planktonic cells in the corrosion cell. The MIC experiments with biofilm were carried out on Day 14 and Day 27.

Electrochemical Analysis. All electrochemical tests were performed after the system reached stable open circuit potential (OCP). The electrochemical data were analyzed using Gamry Echem analyst software and later exported into the Origin software for plotting. Nondestructive linear polarization resistance (LPR) tests were run in triplicates to calculate corrosion rates by polarizing the working electrode at ±10 mV from its OCP and using a scan rate of 0.125 mV/s and stability value of 0.1 mV/s. The polarization resistance (R_p) was determined from the slope of the potential vs current curve and used to calculate corrosion current (I_{corr}) using the Stern−Geary eq (eq 3). Corrosion rates (mils per year (mpy)) were determined by substituting R_p and I_{corr} values in eq 4.

$$i_{corr} = \frac{\beta_a \beta_c}{(\beta_a + \beta_c)} \times \frac{1}{2.3R_p} = \frac{B}{R_p} \tag{3}$$

where β_a and β_c are the anodic and cathodic Tafel constants, respectively; R_p is the polarization resistance; and B is the Stern−Geary coefficient. The Tafel constants were obtained from Tafel analysis that was carried out with a scan rate of 1 mV/s in the potential range of ±250 mV (vs OCP). The polarization plots for bare Cu and FL-hBN-Cu did not display anticipated Tafel behavior in the potential range of 70−100 mV (Figure 3a). We therefore determined the corrosion rates using a linear region from 30 to 40 mV using eq 4.

$$\text{corrosion rate (mpy)} = \frac{Ki_{corr}(EW)}{\rho A} \tag{4}$$

where the constant $K = 1.288 \times 10^5$ milli-inches is used to obtain corrosion rates in mpy. EW, ρ, and A are the equivalent weight (31.7 g), density (8.94 g/cm^3), and area (1 cm^2) of the Cu specimen, respectively. The protection efficiency was calculated by substituting the values of current density obtained from Tafel analysis in eq 5.

$$\text{corrosion protection efficiency, } PE(\%) = \frac{(i^0_{corr} - i_{corr})}{i^0_{corr}} 100 \tag{5}$$

where i^0_{corr} and i_{corr} are the corrosion current density in the absence and presence of hBN coatings.

The electrochemical impedance spectroscopy (EIS) tests were carried out at open circuit potential conditions and in the frequency range of 1×10^5 to 0.01 Hz using an AC signal of amplitude ±10 mV. The corrosion protection efficiency was calculated based on eq 6

$$\text{corrosion protection efficiency} = \frac{(R_{corr,coated} - R_{corr,bare})}{R_{corr,coated}} 100 \tag{6}$$

Corrosion Sample Surface Preparation and Analysis. Biofilm and corrosion products formed on the three working electrodes (bare Cu, FL-hBN-Cu and ML-hBN-Cu) were examined using a field-emission scanning electron microscope (FESEM) and confocal laser scanning microscope (CLSM). Before microscopy analysis, the samples were fixed by immersing in 2% glutaraldehyde for 2 h at 48 °C, sequentially dehydrating with ethanol solution (25%, 50%, 75%, and 100%) for 5 min each, followed by an overnight drying in a desiccator. FESEM (Zeiss Supra40 variable pressure) was used to analyze the surface morphology of biofilm and corrosion products. The SEM images were obtained using secondary electron imaging operated at an accelerated voltage of 3 kV. Biofilm thickness was measured using 3D mode confocal laser scanning microscopy (CLSM) (model solution-treated C2 Plus, Nikon, Tokyo, Japan).

RNA Extraction, cDNA Synthesis, and Real-Time PCR Analysis. Biofilm samples of *D. alaskensis* on the bare Cu, SL-hBN-Cu, and ML-hBN-Cu were slightly washed with phosphate-buffered saline. Cells were then gently scraped using nuclease-free sterile spatula and then transferred immediately to prechilled centrifuge tubes. RNA was extracted using a TRIzol Max Bacterial RNA Isolation Kit (Ambion, Life Technologies) using the manufacturer's protocol and quantified using nanodrop (NanodropTM 1000 spectrophotometer, Thermo Scientific). Following this, 2 μg of dsDNase-treated total RNA was used for cDNA synthesis using a Maxima H Minus First Strand cDNA Synthesis Kit (Thermo Scientific), using the manufacturer's protocol. These cDNA samples were then used as a template for real-time PCR analysis to detect the relative abundance levels of the *tadC* (Flp pilus assembly protein) gene among the biofilm of *D. alaskensis* grown on different materials. For this, gene specific primers (*tadCF*, CATGCTGCTGGGACTGACAT; *tadCR*, ATGATACCCATGCATCCGGC; 16S rRNAF, AAACGACTGCTAATGCCGGA; 16S rRNAR, GCCTTGGTGAGCCATTACCT) were designed and the 16S rRNA gene was used as a housekeeping gene for normalization. For real-time PCR analysis, a reaction was performed that includes 5 μL of 2X PowerUp SYBR Green Master Mix (Thermofisher Scientific), 0.5 μL each of forward and reverse primers (0.4 μM), 2 μL of cDNA template, and 2 μL of nuclease-free water, for a total of 10 μL. Real-time PCR was performed using a QuantStudio 3 Real-Time PCR System (Applied Biosystems) and the relative expression of tadC gene was calculated from their cycle threshold values. The experiment was performed in triplicate for each biological test sample. Nonspecific amplifications were checked using dissociation curves and a no-template control was also maintained as a negative control without the RNA template.

ASSOCIATED CONTENT

Supporting Information

The Supporting Information is available free of charge at https://pubs.acs.org/doi/10.1021/acsnano.0c03625.

SEM, optical microscopic images, and EBSD orientation maps of pristine FL-hBN-Cu and ML-hBN-Cu; grain size and shape analysis using AFM; TEM dark field images of FL-hBN; the electrical equivalent circuit used to fit Nyquist plots, temporal variation in charge-transfer resistance of bare Cu, FL-hBN-Cu, and ML-hBN-Cu; ΔWF at grain vs grain boundaries exposed to the corrodent; details of DFT simulations; Raman spectrum for the pristine hBN and hBN samples exposed to biotic and abiotic corrosion environments; topographic line profile over grain-GB-grain region; electrochemical parameters determined from potentiodynamic polarization for bare Cu, FL-hBN-Cu, and ML-hBN-Cu in H_2SO_4 and Na_2S medium; EEC parameters for bare Cu, FL-hBN-Cu, and ML-hBN-Cu in planktonic cultures after 14 and 27 days of incubation (PDF)

AUTHOR INFORMATION

Corresponding Authors

Muhammad M. Rahman − *Department of Materials Science and NanoEngineering, Rice University, Houston, Texas 77005, United States;* orcid.org/0000-0003-1374-0561; Email: mr64@rice.edu

Pulickel M. Ajayan − *Department of Materials Science and NanoEngineering, Rice University, Houston, Texas 77005, United States;* orcid.org/0000-0001-8323-7860; Email: ajayan@rice.edu

Venkataramana Gadhamshetty − *Department of Civil and Environmental Engineering, 2-Dimensional Materials for Biofilm Engineering Science and Technology (2DBEST) Center, South Dakota School of Mines and Technology, Rapid City,*

https://dx.doi.org/10.1021/acsnano.0c03625
ACS Nano XXXX, XXX, XXX−XXX

South Dakota 57701, United States; orcid.org/0000-0002-8418-3515; Email: Venkata.Gadhamshetty@sdsmt.edu

Authors

Govind Chilkoor − *Department of Civil and Environmental Engineering, 2-Dimensional Materials for Biofilm Engineering Science and Technology (2DBEST) Center, South Dakota School of Mines and Technology, Rapid City, South Dakota 57701, United States*

Kalimuthu Jawaharraj − *Department of Civil and Environmental Engineering, South Dakota School of Mines and Technology, Rapid City, South Dakota 57701, United States*

Bhuvan Vemuri − *Department of Civil and Environmental Engineering, South Dakota School of Mines and Technology, Rapid City, South Dakota 57701, United States*

Alex Kutana − *Department of Materials Science and NanoEngineering, Rice University, Houston, Texas 77005, United States;* orcid.org/0000-0001-6405-6466

Manoj Tripathi − *Department of Physics and Astronomy, University of Sussex, Brighton BN1 9RH, United Kingdom;* orcid.org/0000-0002-8052-428X

Divya Kota − *Department of Nanoscience and Nanoengineering, South Dakota School of Mines and Technology, Rapid City, South Dakota 57701, United States*

Taib Arif − *Department of Mechanical and Industrial Engineering, University of Toronto, Toronto, Ontario M5S3G8, Canada;* orcid.org/0000-0002-3180-9238

Tobin Filleter − *Department of Mechanical and Industrial Engineering, University of Toronto, Toronto, Ontario M5S3G8, Canada;* orcid.org/0000-0003-2609-4773

Alan B. Dalton − *Department of Physics and Astronomy, University of Sussex, Brighton BN1 9RH, United Kingdom;* orcid.org/0000-0001-8043-1377

Boris I. Yakobson − *Department of Materials Science and NanoEngineering, Rice University, Houston, Texas 77005, United States*

M. Meyyappan − *Center for Nanotechnology, NASA Ames Research Center, Mountain View, California 94035, United States*

Complete contact information is available at: https://pubs.acs.org/10.1021/acsnano.0c03625

Notes

The authors declare no competing financial interest.

ACKNOWLEDGMENTS

We acknowledge National Science Foundation CAREER award (1454102), NSF RII T-1 FEC award 1849206, NSF RII T-2 FEC award 1920954 and in part from NASA (NNX16AQ98A) for funding this research. A.K. and B.I.Y. acknowledge the U.S. Department of Energy, Fossil Energy Program, Division of Crosscutting R&D and Systems Integration contract DE-AC05-00OR22725 with UT-Battelle (grant 4000174979), and the R. Welch Foundation (C-1590). M.T. and A.B.D acknowledge the University of Sussex strategic development fund.

REFERENCES

(1) Jacobs, S.; Reiber, S.; Edwards, M. Sulfide-Induced Copper Corrosion. *J. - Am. Water Works Assoc.* **1998**, *90*, 62−73.

(2) Facciotti, M.; Amaro, P. S.; Brown, R. C. D.; Lewin, P. L.; Pilgrim, J. A.; Wilson, G.; Jarman, P. N.; Fletcher, I. W. Static Secondary Ion Mass Spectrometry Investigation of Corrosion Inhibitor Irgamet®39 on Copper Surfaces Treated in Power Transformer Insulating Oil. *Corros. Sci.* **2015**, *98*, 450−456.

(3) Salahinejad, E.; Eslami-Farsani, R.; Tayebi, L. Corrosion Failure Analysis of Printed Circuit Boards Exposed to H_2S-Containing Humid Environments. *Eng. Failure Anal.* **2017**, *79*, 538−546.

(4) Vargas, I. T.; Fischer, D. A.; Alsina, M. A.; Pavissich, J. P.; Pastén, P. A.; Pizarro, G. E. Copper Corrosion and Biocorrosion Events in Premise Plumbing. *Materials* **2017**, *10*, 1036.

(5) Kopteva, Z. P.; Zanina, V. V.; Kozlova, I. A. Microbial Corrosion of Protective Coatings. *Surf. Eng.* **2004**, *20*, 275−280.

(6) Videla, H. A.; Herrera, L. K. Microbiologically Influenced Corrosion: Looking to the Future. *Int. Microbiol.* **2005**, *8*, 169−180.

(7) Kotakoski, J.; Krasheninnikov, A. V.; Kaiser, U.; Meyer, J. C. From Point Defects in Graphene to Two-Dimensional Amorphous Carbon. *Phys. Rev. Lett.* **2011**, *106*, 105505.

(8) Yazyev, O. V.; Chen, Y. P. Polycrystalline Graphene and Other Two-Dimensional Materials. *Nat. Nanotechnol.* **2014**, *9*, 755−767.

(9) Xu, Z.; Gao, C. *In Situ* Polymerization Approach to Graphene-Reinforced Nylon-6 Composites. *Macromolecules* **2010**, *43*, 6716−6723.

(10) Krishnamurthy, A.; Gadhamshetty, V.; Mukherjee, R.; Chen, Z.; Ren, W.; Cheng, H. M.; Koratkar, N. Passivation of Microbial Corrosion Using a Graphene Coating. *Carbon* **2013**, *56*, 45−49.

(11) Prasai, D.; Tuberquia, J. C.; Harl, R. R.; Jennings, G. K.; Bolotin, K. I. Graphene: Corrosion-Inhibiting Coating. *ACS Nano* **2012**, *6*, 1102−1108.

(12) Sommerfeld Ross, S.; Tu, M. H.; Falsetta, M. L.; Ketterer, M. R.; Kiedrowski, M. R.; Horswill, A. R.; Apicella, M. A.; Reinhardt, J. M.; Fiegel, J. Quantification of Confocal Images of Biofilms Grown on Irregular Surfaces. *J. Microbiol. Methods* **2014**, *100*, 111−120.

(13) Mahvash, F.; Eissa, S.; Bordjiba, T.; Tavares, A. C.; Szkopek, T.; Siaj, M. Corrosion Resistance of Monolayer Hexagonal Boron Nitride on Copper. *Sci. Rep.* **2017**, *7*, 1−5.

(14) Parra, C.; Montero-Silva, F.; Henríquez, R.; Flores, M.; Garín, C.; Ramírez, C.; Moreno, M.; Correa, J.; Seeger, M.; Häberle, P. Suppressing Bacterial Interaction with Copper Surfaces through Graphene and Hexagonal-Boron Nitride Coatings. *ACS Appl. Mater. Interfaces* **2015**, *7*, 6430−6437.

(15) Li, L. H.; Cervenka, J.; Watanabe, K.; Taniguchi, T.; Chen, Y. Strong Oxidation Resistance of Atomically Thin Boron Nitride Nanosheets. *ACS Nano* **2014**, *8*, 1457−1462.

(16) Yan, K.; Lee, H.-W.; Gao, T.; Zheng, G.; Yao, H.; Wang, H.; Lu, Z.; Zhou, Y.; Liang, Z.; Liu, Z.; Chu, S.; Cui, Y. Ultrathin Two-Dimensional Atomic Crystals as Stable Interfacial Layer for Improvement of Lithium Metal Anode. *Nano Lett.* **2014**, *14*, 6016−6022.

(17) Jenkins, H. D. B.; Thakur, K. P. Reappraisal of Thermochemical Radii for Complex Ions. *J. Chem. Educ.* **1979**, *56*, 576.

(18) Barrett, J.. *Inorganic Chemistry in Aqueous Solution*; Royal Society of Chemistry, 2003.

(19) Chilkoor, G.; Karanam, S. P.; Star, S.; Shrestha, N.; Sani, R. K.; Upadhyayula, V. K. K.; Ghoshal, D.; Koratkar, N. A.; Meyyappan, M.; Gadhamshetty, V. Hexagonal Boron Nitride: The Thinnest Insulating Barrier to Microbial Corrosion. *ACS Nano* **2018**, *12*, 2242−2252.

(20) Kim, S. M.; Hsu, A.; Park, M. H.; Chae, S. H.; Yun, S. J.; Lee, J. S.; Cho, D.-H.; Fang, W.; Lee, C.; Palacios, T.; Dresselhaus, M.; Kim, K. K.; Lee, Y. H.; Kong, J. Synthesis of Large-Area Multilayer Hexagonal Boron Nitride for High Material Performance. *Nat. Commun.* **2015**, *6*, 1−11.

(21) Kim, K. K.; Hsu, A.; Jia, X.; Kim, S. M.; Shi, Y.; Dresselhaus, M.; Palacios, T.; Kong, J. Synthesis and Characterization of Hexagonal Boron Nitride Film as a Dielectric Layer for Graphene Devices. *ACS Nano* **2012**, *6*, 8583−8590.

(22) Gorbachev, R. V.; Riaz, I.; Nair, R. R.; Jalil, R.; Britnell, L.; Belle, B. D.; Hill, E. W.; Novoselov, K. S.; Watanabe, K.; Taniguchi, T.; Geim, A. K.; Blake, P. Hunting for Monolayer Boron Nitride: Optical and Raman Signatures. *Small* **2011**, *7*, 465−468.

(23) Otsuka, R.; Uda, M. Cathodic Corrosion of Cu in H_2SO_4. *Corros. Sci.* **1969**, *9*, 703−IN27.

(24) Hu, S.; Lozada-Hidalgo, M.; Wang, F. C.; Mishchenko, A.; Schedin, F.; Nair, R. R.; Hill, E. W.; Boukhvalov, D. W.; Katsnelson, M. I.; Dryfe, R. a. W.; Grigorieva, I. V.; Wu, H. A.; Geim, A. K. Proton Transport through One-Atom-Thick Crystals. *Nature* **2014**, *516*, 227−230.
(25) Zaafarany, I.; Boller, H. Corrosion of Copper Electrode in Sodium Sulfide Solution. *J. Saudi Chem. Soc.* **2010**, *14*, 183−189.
(26) Pease, R. S. Crystal Structure of Boron Nitride. *Nature* **1950**, *165*, 722−723.
(27) Borisova, D.; Antonov, V.; Proykova, A. Hydrogen Sulfide Adsorption on a Defective Graphene. *Int. J. Quantum Chem.* **2013**, *113*, 786−791.
(28) Xu, L. C.; Chan, K. Y.; Fang, H. H. P. Application of Atomic Force Microscopy in the Study of Microbiologically Influenced Corrosion. *Mater. Charact.* **2002**, *48*, 195−203.
(29) Preedy, E.; Perni, S.; Nipiĉ, D.; Bohinc, K.; Prokopovich, P. Surface Roughness Mediated Adhesion Forces between Borosilicate Glass and Gram-Positive Bacteria. *Langmuir* **2014**, *30*, 9466−9476.
(30) Husain, E.; Narayanan, T. N.; Taha-Tijerina, J. J.; Vinod, S.; Vajtai, R.; Ajayan, P. M. Marine Corrosion Protective Coatings of Hexagonal Boron Nitride Thin Films on Stainless Steel. *ACS Appl. Mater. Interfaces* **2013**, *5*, 4129−4135.
(31) Krumholz, L. R.; Bradstock, P.; Sheik, C. S.; Diao, Y.; Gazioglu, O.; Gorby, Y.; McInerney, M. J. Syntrophic Growth of *Desulfovibrio alaskensis* Requires Genes for H_2 and Formate Metabolism as Well as Those for Flagellum and Biofilm Formation. *Appl. Environ. Microbiol.* **2015**, *81*, 2339−2348.
(32) Wikieł, A. J.; Datsenko, I.; Vera, M.; Sand, W. Impact of *Desulfovibrio alaskensis* Biofilms on Corrosion Behaviour of Carbon Steel in Marine Environment. *Bioelectrochemistry* **2014**, *97*, 52−60.
(33) Beech, I. B.; Cheung, C. W. S. Interactions of Exopolymers Produced by Sulphate-Reducing Bacteria with Metal Ions. *Int. Biodeterior. Biodegrad.* **1995**, *35*, 59−72.
(34) Beech, I. B.; Sunner, J. A.; Hiraoka, K. Microbe-Surface Interactions in Biofouling and Biocorrosion Processes. *Int. Microbiol.* **2005**, *8*, 157−168.
(35) Naghdi, S.; Sanchez-Arriaga, G.; Rhee, K. Y. Tuning the Work Function of Graphene toward Application as Anode and Cathode. *J. Alloys Compd.* **2019**, *805*, 1117−1134.
(36) Zhang, K.; Feng, Y.; Wang, F.; Yang, Z.; Wang, J. Two-Dimensional Hexagonal Boron Nitride (2D-HBN): Synthesis, Properties and Applications. *J. Mater. Chem. C* **2017**, *5*, 11992−12022.

https://dx.doi.org/10.1021/acsnano.0c03625
ACS Nano XXXX, XXX, XXX−XXX